

Crystal structure and functional mechanism of a human antimicrobial membrane channel

Chen Song^a, Conrad Weichbrodt^b, Evgeniy S. Salnikov^c, Marek Dynowski^{d,e}, Björn O. Forsberg^a, Burkhard Bechinger^c, Claudia Steinem^b, Bert L. de Groot^a, Ulrich Zachariae^{f,1}, and Kornelius Zeth^{e,g,1}

^aComputational Biomolecular Dynamics Group, Max Planck Institute for Biophysical Chemistry, 37077 Göttingen, Germany; ^bInstitute for Organic and Biomolecular Chemistry, Georg August University Göttingen, 37077 Göttingen, Germany; ^cMembrane Biophysics and NMR, Chemistry Institute, Unité Mixte de Recherche 7177, University of Strasbourg and Centre National de la Recherche Scientifique, 67000 Strasbourg, France; ^dResearch and Development, Computing Centre, Freiburg University, 79104 Freiburg, Germany; ^eMax Planck Institute for Developmental Biology, 72076 Tübingen, Germany; ^fScottish Universities' Physics Alliance, School of Physics and Astronomy, The University of Edinburgh, Edinburgh EH9 3JZ, United Kingdom; and ^gUnidad de Biofísica, University of Basque Country and Spanish Science Research Council, 48940 Leioa, Vizcaya, Spain

Edited by Wolfgang Baumeister, Max-Planck Institute of Biochemistry, Martinsried, Germany, and approved January 16, 2013 (received for review August 28, 2012)

Multicellular organisms fight bacterial and fungal infections by producing peptide-derived broad-spectrum antibiotics. These host-defense peptides compromise the integrity of microbial cell membranes and thus evade pathways by which bacteria develop rapid antibiotic resistance. Although more than 1,700 host-defense peptides have been identified, the structural and mechanistic basis of their action remains speculative. This impedes the desired rational development of these agents into next-generation antibiotics. We present the X-ray crystal structure as well as solid-state NMR spectroscopy, electrophysiology, and MD simulations of human dermcidin in membranes that reveal the antibiotic mechanism of this major human antimicrobial, found to suppress *Staphylococcus aureus* growth on the epidermal surface. Dermcidin forms an architecture of high-conductance transmembrane channels, composed of zinc-connected trimers of antiparallel helix pairs. Molecular dynamics simulations elucidate the unusual membrane permeation pathway for ions and show adjustment of the pore to various membranes. Our study unravels the comprehensive mechanism for the membrane-disruptive action of this mammalian host-defense peptide at atomistic level. The results may form a foundation for the structure-based design of peptide antibiotics.

crystallography | electrophysiology | ion conduction | molecular dynamics

Host-defense peptides actively control a wide range of microbes across most tissues of the animal and plant kingdoms, which signifies their importance during the evolution of multicellular organisms (1–3). In comparison with traditional small-molecule antibiotics, host-defense or antimicrobial peptides (AMPs) are often considered to have a distinctly superior property, as they target the microbial Achilles heel, i.e., the unique but essential features of all microbial cellular membranes (albeit at somewhat lower efficacy) (1–5). Thus, microbes have not been able to develop efficient resistance mechanisms against AMPs within the time frame of their parallel evolution (3, 5).

In recent years, a steep global rise in infections by multi-resistant bacteria such as methicillin-resistant *Staphylococcus aureus* (MRSA) has been recorded (6, 7). These often affect the patients' skin and epithelial injuries, and are particularly hard to treat with conventional small-molecule antibiotics (8). The development of high-efficiency antibiotic agents, less prone to evoking resistance, is thus essential (4–7). However, the rational design of AMPs requires a detailed understanding of their structural and mechanistic determinants of antimicrobial action, which has not been achieved to date (4, 9, 10). The lack of molecular-based understanding has been named as the main obstacle hampering progress in this field (11).

The human epithelium exposes a large external surface for the growth of microbes (12). Among the major AMPs detected on human skin is the negatively charged peptide dermcidin (DCD; refs. 13–15), which is constitutively produced in sweat glands as

a precursor protein, further processed and finally secreted into human sweat (refs. 13 and 16; Fig. S1 A–C). DCD is active against a broad spectrum of bacteria including MRSA and rifampin- and isoniazid-resistant *Mycobacterium tuberculosis* at concentrations of $\sim 1 \mu\text{g/mL}$ (16). Its antimicrobial activity is particularly robust against changes in pH and ionic strength (13, 16). When isolated from sweat or after recombinant expression, DCD forms an equilibrium mixture of oligomers of varying size, both in solution and in membrane mimetics (16, 17). Human sweat is enriched in divalent ions, among which Zn^{2+} is of particular importance and has previously been demonstrated to be essential for AMP action on some microbes (18, 19).

AMPs are classified according to their overall charge, secondary structure, and more specifically the presence of certain amino acid combinations such as cysteines or prolines (1, 9). Many AMPs carry an excess of positive charges to interact favorably with the negatively charged surface of bacterial membranes (1–3). Although a number of models for the membrane-disrupting action of AMPs have been proposed, detailed and compelling structural and mechanistic evidence for any of these models involving mammalian (or human) AMPs has so far been elusive (4, 9, 10). To elucidate the antibiotic mechanism of DCD and reveal the underlying structural determinants, including the level of oligomerization, we crystallized the 48-residue DCD peptide (Fig. S1A), determined its channel-forming structure, and looked at membrane interaction with solid-state (ss) NMR spectroscopy. We then conducted electrophysiology experiments in which we characterized the activity of DCD in membranes under various conditions. The experimental results are in excellent agreement with data we obtained from extended computational electrophysiology and molecular dynamics (MD) simulations of the channel assembly, which further reveal the ion-transfer mechanism of DCD in atomic detail.

Results

Structural Architecture of the Hexameric AMP Channel. The structure of assembled DCD solved at 2.5-Å resolution exhibits a channel architecture comprising a hexameric bundle formed by

Author contributions: C. Song, B.B., C. Steinem, B.L.d.G., U.Z., and K.Z. designed research; C. Song, C.W., E.S.S., M.D., B.O.F., and K.Z. performed research; C. Song, C.W., E.S.S., B.O.F., B.B., C. Steinem, B.L.d.G., U.Z., and K.Z. analyzed data; and C. Song, E.S.S., B.B., C. Steinem, B.L.d.G., U.Z., and K.Z. wrote the paper.

The authors declare no conflict of interest.

This article is a PNAS Direct Submission.

Freely available online through the PNAS open access option.

Data deposition: The atomic coordinates and structure factors have been deposited in the Protein Data Bank, www.pdb.org (PDB ID code 2YMK).

¹To whom correspondence may be addressed. E-mail: uzachari@ph.ed.ac.uk or kornelius.zeth@googlemail.com.

This article contains supporting information online at www.pnas.org/lookup/suppl/doi:10.1073/pnas.1214739110/-DCSupplemental.

elongated α -helices, which adopts overall dimensions of $\sim 8 \times 4$ nm (Fig. 1A). Channel formation involves trimerization of antiparallel peptide dimers resulting in a firmly enclosed channel structure. Each monomer presents two distinct interfaces to neighboring subunits (Fig. 1A). The extended interface, displaying a contact surface of 930 \AA^2 , is mainly formed by salt bridges, and the second interface covers 520 \AA^2 (IF1) and is primarily stabilized by Zn^{2+} ions that intercalate between the two helices (Fig. 1A and Fig. S1D). The zinc ions in DCD are coordinated by *N*- and *C*-terminal residues of dimerizing peptides (residues involved: Glu5, Glu9, His38', and Asp42') (Fig. 1A and B). They are attached to the inner wall of the channel and substantially change the overall charge of the assembly (from $-12e$ to neutral). In addition, they modify the local charge distribution especially at the entrance of the channel.

DCD shows a unique distribution of charges, reflecting peptide oligomers that occur both in soluble and membrane-bound forms. The entire hexameric channel comprises 96 ionizable residues, which are all oriented toward the channel interior (Fig. 1C, F, and G). This enormous charge density, which is not completely shielded to the exterior, is likely to contribute to the relatively high aqueous solubility of DCD. The inner space of the peptide channel has an apparent separation into five radially symmetric charge girdles I/II/III/II/I (Fig. 1C). Residues facing

the acyl chain region of the membrane are exclusively hydrophobic (Ala, Val, Leu) (Fig. 1D and Fig. S1A). However, no aromatic residues are found that are commonly considered to be important for the lateral adjustment of proteins in membranes (20, 21). The channel diameter is not homogeneous and varies along the *y* axis with two rather narrow entry sites, followed by a widened interior with windowlike eyelets in the IF1 interface (Fig. 1A, E, and H). The six lateral openings have a diameter of ~ 1 nm and are surrounded by small amino acids as well as positively charged residues that may have an influence on the selection of ion entry. The distance between two adjacent eyelets is 2.5 (same plane) and 3 nm (opposite plane), respectively, roughly corresponding to the width of the membrane hydrophobic core.

Interaction of DCD with Lipid Bilayers. To investigate the interaction of DCD with bilayers, we conducted ss-NMR spectroscopy experiments. The structural preferences of DCD were investigated after labeling of the peptide with ^{15}N at the Gly22 position and $^2\text{H}_3$ -Ala at position 25, its reconstitution into oriented lipid bilayers and investigation by proton-decoupled ^{15}N ss-NMR spectroscopy. DCD labeled with ^{15}N at Gly22 exhibits a ^{15}N chemical shift of (62 ± 2) ppm in oriented 1-palmitoyl-2-oleoyl-*sn*-glycero-3-phosphoethanolamine/1-palmitoyl-2-oleoyl-

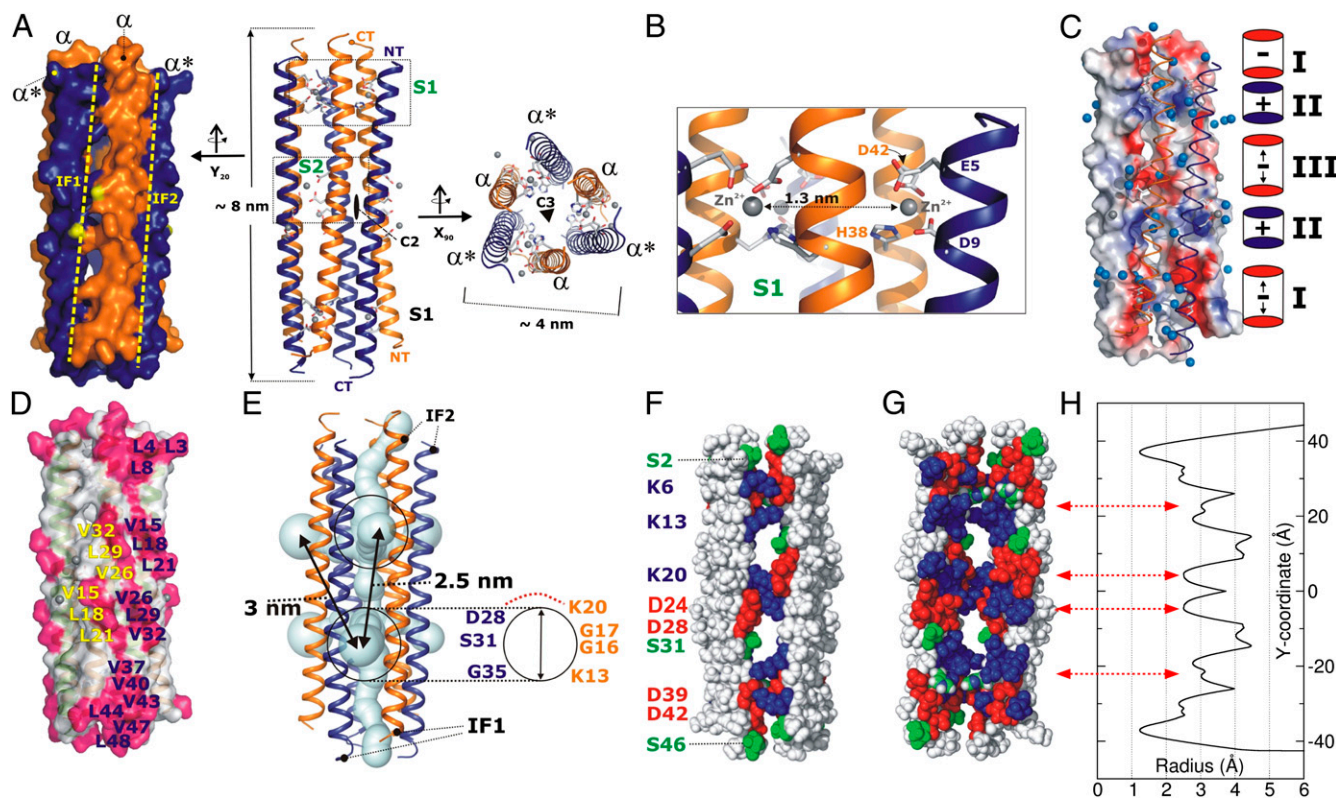


Fig. 1. Crystal structure and surface characteristics of the human dermcidin channel. (A) X-ray structure of the hexameric DCD channel shown in cartoon representation from the side and top (*Middle and Right*), and as surface representation (*Left*). The different orientations of the individual peptides relative to the membrane normal are marked in orange and dark blue, and termini are marked (NT, N terminus; CT, C terminus). Arrows combined with tilt angle and axes give the relative orientation. Residues involved in Zn binding are shown in stick representation and Zn ions are marked in gray. The symmetry axis of the channel is marked with C2 (for the side view) and C3 (for the top view). Two interfaces of different surface area are formed after trimerization and named IF1 and IF2. (B) Close-up into the Zn-binding site S1. Four residues (Glu5 and Asp11 from one peptide and Asp41 and His38 from the second) form each Zn-binding site. The distance between the Zn ions is marked by arrows. (C) Electrostatic surface representation of the channel with two monomers marked in ribbon representation. The channel comprises five alternating patches of elongated negative (red) and ring-like positive (blue) charge. (D) Side view of DCD (hydrophobic residues in magenta). (E) Ribbon model of DCD. The pore diameter is represented by spheres. The lateral entry points are marked with circles. (F) Hydrophilic residues on the trimeric interface (negatively charged residues in red, positively charged residues in blue, polar residues in green). Nonpolar residues are shown in white. (G) The hydrophilic channel interior. For clarity, the front dimer is omitted; colors as in F. (H) Channel radius along the pore axis.

sn-glycero-3-phospho(1'-*rac*-glycerol) (POPE/POPG, 3:1) membranes both in the absence or presence of a 10-fold excess of Zn^{2+} (Fig. 2 *A* and *B*). This indicates an in-planar alignment of the major population of the labeled peptide domain (22), in agreement with previous oriented circular dichroism data (16). The chemical shifts are within experimental error identical in POPE/POPG, 1-palmitoyl-2-oleoyl-*sn*-glycero-3-phosphocholine, and DPhPC/cholesterol 9:1 membranes and also independent of zinc ions (ZnCl_2 salt) and the sample preparation protocol. The ^2H ss-NMR spectrum of the $^2\text{H}_3$ -Ala25 labeled site exhibits a ^2H quadrupolar splitting of (45 ± 3) kHz (Fig. 2*C*) and further restricts the tilt and pitch angle (23). A detailed topological analysis is shown by the red and black traces in Fig. S2 for the ^{15}N chemical shift and the ^2H quadrupolar splitting, respectively (see ref. 23). Both NMR parameters agree when their corresponding traces intersect leading to a set of tilt/pitch angular pairs in the proximity of $(90^\circ/90^\circ)$, which would represent an ideal alignment of the amphipathic helix with the membrane interface (Fig. 2*B*). In agreement, the ^2H spectra of the fatty acyl chains show pronounced membrane disordering by the presence of DCD (Fig. S3).

Functional Properties of the Channel Highlight the Importance of Zinc as Cofactor. The solid-state NMR data represent probably the lowest energy state after extensive equilibration of the major population of the peptide and, in particular, in the absence of a membrane potential. In contrast, electrophysiological recordings monitor a population that may occur as a minor, but functionally relevant, species under the application of a transmembrane voltage. To obtain functional evidence for the activity of DCD channels in the membrane, we collected conductivity data in planar lipid bilayers. First, membranes were prepared in 1 M NaCl, 5 mM Hepes, pH 7.1 in the absence of Zn^{2+} . After the addition of DCD

in micromolar concentrations, two out of the six membranes showed weak activity of the peptide (Fig. 2*D*). Altogether, only 20 current steps were observed, from which a mean conductance of $G = (31 \pm 8)$ pS was evaluated.

By contrast, in the presence of Zn^{2+} , the addition of DCD at concentrations of 850 nM or higher resulted in current fluctuations for every membrane preparation, which eventually led to rupture of the membrane (Fig. 2*E* and *F*). These concentrations are similar to DCD concentrations used to efficiently remove bacteria in antimicrobial assays. Evaluation of 1,009 events revealed a mean conductance of $G = (81 \pm 14)$ pS (Fig. 2*G*) and the mean open lifetime was determined to be $\tau = (4.4 \pm 0.2)$ ms (Fig. 2*H*). This shows that, in the presence of zinc ions, specific and individual channels with a defined conductance are formed in the membrane bilayer. Neither the membrane with DCD alone nor the addition of only Zn^{2+} gave rise to the occurrence of individual channels in the electrophysiology experiments. However, we found that the polarity of the electric field had a significant impact on the efficiency of DCD- Zn^{2+} insertion.

To further investigate the importance of the specific Zn^{2+} interactions and their impact on the active membrane-bound form of DCD, we mutated His38, one of the main interaction partners of DCD with Zn^{2+} , to alanine and studied this mutant through electrophysiology. The single mutation was sufficient to abolish channel formation in membranes (Fig. S4). This finding is most compatible with the notion that the assembled structure, which is characterized by specific Zn^{2+} -conferred peptide-peptide interactions, is the most prominent membrane-disruptive form. It is important to note that the current fluctuations seen for DCD- Zn^{2+} in electrophysiology are representative of a small number of channels efficiently conducting ions across membranes,

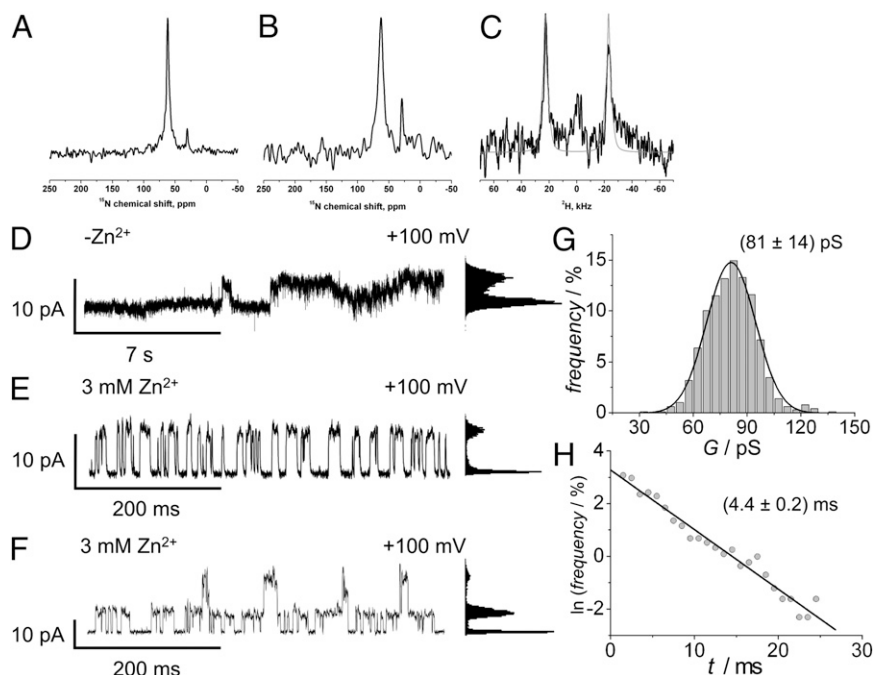


Fig. 2. Electrophysiology and ss-NMR of DCD in the presence and absence of zinc ions. (*A* and *B*) Proton-decoupled ^{15}N and (*C*) ^2H ss-NMR spectra of 2 mol % [^{15}N -Gly22, $^2\text{H}_3$ -Ala25]-DCD in oriented POPE/POPG without ZnCl_2 (*A*) and with fivefold molar excess of ZnCl_2 relative to the peptide concentration (*B* and *C*). $^{15}\text{NH}_4\text{Cl}$ (40.0 ppm) and $^2\text{H}_2\text{O}$ (0 Hz) were used as external references and the spectra processed with an exponential line broadening of 50 (*A* and *B*) and 500 Hz (*C*), respectively. The gray line in *C* shows a simulated spectrum arising from a 3° Gaussian distribution for the peptide alignment and a spectral line width of 2 kHz. (*D*) Current trace and point amplitude histogram representing DCD activity in 1 M NaCl, 5 mM Hepes, pH 7.1 recorded at a holding potential of +100 mV. Protein activity was only rarely observed under these conditions. (*E* and *F*) Current traces and point amplitude histograms of DCD-1L in 1 M NaCl, 3 mM ZnCl_2 , 5 mM Hepes, pH 7.1 recorded at a holding potential of +100 mV; (*E*) 3.3 μM DCD-1L was added resulting in one defined conductance state. In (*F*) 7.9 μM DCD-1L was used and two distinct conductance levels each of about 80 pS were monitored, suggesting the insertion of two channels. (*G*) An event histogram of the conductance levels ($n = 1,009$) shows a mean conductance of $G = (81 \pm 14)$ pS. (*H*) Open lifetime analysis with $\tau = (4.4 \pm 0.2)$ ms.

Here, we present a comprehensive functional mechanism of a human antimicrobial peptide in its active form, including its high-resolution structure, single-channel functional measurements, and atomistic simulations of permeation. In the absence of transmembrane voltage (TMV), in-plane alignments have been observed for DCD and other helical antimicrobial peptides such as magainins or cecropins (Fig. 2 A–C; reviewed in ref. 35). However, important differences exist between the latter peptides and DCD, already when their size and charge are compared. Of note is that when TMV is applied, the channel recordings reveal mostly membrane lysis in the case of magainins or cecropins, and only rarely are the stepwise conduction increases clearly observed with DCD. The electrophysiological recordings of lysis or stochastic membrane deformations, however, are erratic, highly variable, and characterized by considerable fluctuations. Therefore, it is likely that the tilted hexamer of DCD provides an example for a hitherto undescribed mechanism for the membrane interactions of antimicrobial peptides (for reviews of other mechanisms, see ref. 36). The ensemble of data from the herein and previously presented studies (16) suggest that DCD occurs in a number of states that are interconnected by sensitive equilibria as illustrated in Fig. 4, including oligomers and monomers in solution, as well as monomers or small oligomers lying parallel to the membrane surface (Fig. 2 A–C). Furthermore, transmembrane potentials and the presence of Zn^{2+} , by neutralizing the anionic charges of the DCD polypeptides, favor the formation of oligomeric structures spanning the membrane (Fig. 2 D–H). These channels display a conductance of about 80 to 110 pS.

Although the suggested mechanisms of AMP action have so far remained largely speculative (4, 9, 10), our study on DCD provides a structurally detailed and experimentally validated mechanism for membrane perturbation by an AMP. It is striking that none of the currently debated models explicitly predict this channel. Our X-ray, electrophysiology, and simulation data show a barrel-stave-like channel (10), which is held together by divalent

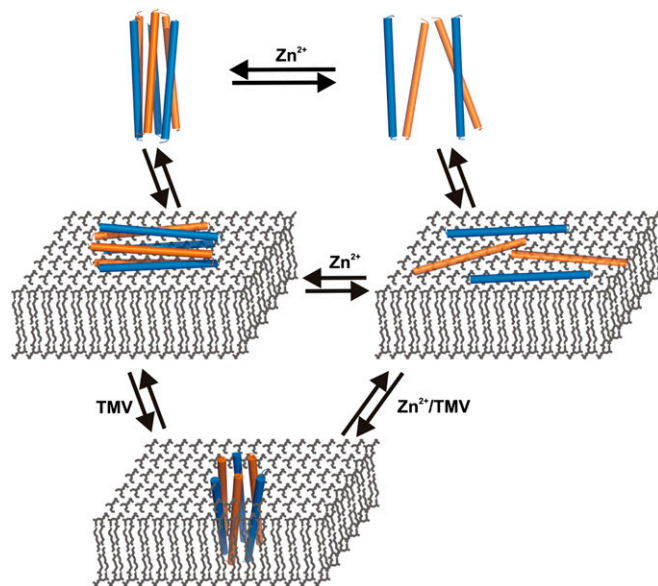


Fig. 4. Model of DCD interactions with membranes. Peptide monomers of DCD are in equilibrium with the hexameric channel form, which is stabilized by the presence of zinc. The channel and DCD monomers can interact with membrane surfaces through lateral association as shown by our NMR studies. The channel can be translocated into the membrane upon application of a TMV, as shown in planar lipid membrane conductance measurements, and forms a representative of the barrel-stave model. Once the channel is integrated into a membrane, channel conductance can be recorded by planar lipid membrane experiments and estimated by molecular dynamics studies.

cations and displays a high permeability for water and ions, as ions can enter and exit through side eyelets of a tilted pore. DCD thereby forms a site of severe membrane disruption. As recently noted, a single ion channel with a conductance near 100 pS can dissipate the bacterial transmembrane potential on a time scale of as little as 10^{-4} s (37). The DCD channel characterized here thus represents highly efficient channels, and even a few of which are capable of rapidly abrogating the bacterial transmembrane potential that is essential for cell survival. Its structure and functional mechanism may form a foundation for the rational design of antibacterial, peptide-derived drugs that are less liable to evoke resistance.

Material and Methods

Crystallization and Structure Determination. The DCD peptide sequence (Fig. S1) was synthesized by the company Peptide2.0 (www.peptide2.com) to yield a product of >97% purity. For crystallization, the peptide was solved in 10 mM Hepes at a concentration of 50 mg/mL (~10 mM final concentration). Crystallization drops were prepared by mixing 400 nL of the peptide solution with the same amount of reservoir, and drops were incubated by vapor diffusion (sitting drops) under a variety of different conditions (800 conditions from Qiagen screens). Two conditions, both of which contained Zn-acetate, yielded crystals suitable for X-ray diffraction analysis. Crystals for X-ray diffraction were taken from a drop containing 0.2 M Zn(ac)₂, 0.1 M Na-cacodylate, 18% (wt/vol) PEG8000 at pH 6.5. The channel has been crystallized in the absence of lipophilic molecules such as detergents or lipids. Crystals were taken from the mother liquor and flash-frozen in liquid nitrogen without adding cryoprotectant. Data were collected at the Swiss Light Source, beamline PXII at 100 K and 20 eV above the theoretical Zn-edge (9.658 keV). Three hundred sixty 1° images were collected at 2% beam intensity to generate a highly redundant dataset for single anomalous dispersion data processing. Diffraction data were processed with XDS/XSCALE (38). The structure was solved with the Phenix program package (39) with Phaser (38) for heavy atom detection and Resolve (40) for initial solvent flattening. Solvent flattening was repeated by Pirate of the CCP4 suite (41) and a model 85% complete was built with Buccaneer (42). The final model was obtained after several rounds of manual rebuilding and refinement with Coot (43), REFMAC (44), and PHENIX (39). For more details see *SI Materials and Methods* and Table S1.

Solid-State NMR Spectroscopy. Samples were prepared by dissolving 4 mg of peptide and ~30 mg of lipid in TFE/water 50/50 vol/vol, dried in air and under high vacuum, applied onto 20 ultra-thin cover glasses, and equilibrated at 93% relative humidity, as described previously (45). Where appropriate, ZnCl₂ was added in five- to ten-fold molar excess over the peptide. As an alternate, peptide and ZnCl₂ were added to preformed vesicles, and the resulting mixture was applied onto the glass plates (45). The ss-NMR spectra were recorded on a Bruker Avance wide-bore NMR spectrometer operating at 9.4 T with flat-coil probes as described previously (46). Orientational restraints were calculated from the solid-state NMR spectra as described in (46) by using the chemical shift tensor (44, 65, 211) ppm, a maximum quadrupolar splitting of 74 kHz for the alanine ²H₃C group and DCD coordinates from the crystal structure. For further details of ss-NMR methods and data analysis see *SI Materials and Methods*.

Electrophysiology. Giant unilamellar vesicles (GUVs) composed of DPhPC/cholesterol (9:1) were prepared by the electroformation method with a 3-V peak-to-peak AC voltage at a frequency of 5 Hz for 2 h at 20 °C in the presence of 1 M sorbitol (47–49). A freestanding membrane was prepared by spreading a GUV in 1 M NaCl, 5 mM Hepes, pH 7.1 on an aperture in a borosilicate chip (Port-a-Patch; Nanion Technologies) by applying 15–40-mbar negative pressure resulting in a solvent-free membrane with a resistance in the GΩ range. After successful membrane formation, varying amounts of DCD stock solution (100 μM) were added to 50-μL buffer solution, while applying a DC potential of +100 mV. Current traces were recorded at a sampling rate of 50 kHz using an Axopatch 200B amplifier (Axon Instruments). They were filtered with a low-pass four-pole Bessel filter of 1 kHz and digitized by an A/D converter (Digidata 1322; Axon Instruments). Data evaluation was performed with the pClamp 9 software package (Axon Instruments). For additional details see *SI Materials and Methods*.

Molecular Dynamics and Computational Electrophysiology Simulations. All MD simulations were performed with the GROMACS package, version 4.5 (50) in combination with the CHARMM36 force field (51). Unless otherwise stated, the simulation temperature was 310 K. The protein, lipids, and water/ions

were coupled separately to a temperature bath with the v-rescale method with a time constant of 0.1 ps (52). Short-range electrostatics were calculated with a cutoff of 1.3 nm. Long-range electrostatics were treated with the particle-mesh Ewald method (53). Short-range Van der Waals (VdW) interactions were calculated explicitly up to a distance of 0.8 nm, beyond which a switch function was used to smoothly switch off the VdW interactions to reach 0 at 1.2 nm. All bonds were constrained using the LINCS method (54). The time step was 2 fs for all-atom MD simulations and 4 fs for simulations with the virtual site model for hydrogen atoms (55), respectively. To study whether the oligomer is ion conductive, we used the computational electrophysiology method (26). For additional details see *SI Materials and Methods*.

- Zaslouff M (2002) Antimicrobial peptides of multicellular organisms. *Nature* 415(6870):389–395.
- Hancock RE, Diamond G (2000) The role of cationic antimicrobial peptides in innate host defences. *Trends Microbiol* 8(9):402–410.
- Peschel A, Sahl H-G (2006) The co-evolution of host cationic antimicrobial peptides and microbial resistance. *Nat Rev Microbiol* 4(7):529–536.
- Fjell CD, Hiss JA, Hancock REW, Schneider G (2012) Designing antimicrobial peptides: Form follows function. *Nat Rev Drug Discovery* 11(1):37–51.
- Hancock REW, Sahl H-G (2006) Antimicrobial and host-defense peptides as new anti-infective therapeutic strategies. *Nat Biotechnol* 24(12):1551–1557.
- Spellberg B, et al.; Infectious Diseases Society of America (2008) The epidemic of antibiotic-resistant infections: A call to action for the medical community from the Infectious Diseases Society of America. *Clin Infect Dis* 46(2):155–164.
- Bush K, et al. (2011) Tackling antibiotic resistance. *Nat Rev Microbiol* 9(12):894–896.
- Hersh AL, Chambers HF, Maselli JH, Gonzales R (2008) National trends in ambulatory visits and antibiotic prescribing for skin and soft-tissue infections. *Arch Intern Med* 168(14):1585–1591.
- Brogden KA (2005) Antimicrobial peptides: Pore formers or metabolic inhibitors of bacteria? *Nat Rev Microbiol* 3(3):238–250.
- Melo MN, Ferre R, Castanho MA (2009) Antimicrobial peptides: Linking partition, activity and high membrane-bound concentrations. *Nat Rev Microbiol* 7(3):245–250.
- Arouri A, Dathe M, Blume A (2009) Peptide induced demixing in PG/PE lipid mixtures: A mechanism for the specificity of antimicrobial peptides towards bacterial membranes? *Biochim Biophys Acta* 1788(3):650–659.
- Gläser R, et al. (2005) Antimicrobial psoriasin (S100A7) protects human skin from *Escherichia coli* infection. *Nat Immunol* 6(1):57–64.
- Schitteck B, et al. (2001) Dermcidin: A novel human antibiotic peptide secreted by sweat glands. *Nat Immunol* 2(12):1133–1137.
- Ganz T (2003) Defensins: Antimicrobial peptides of innate immunity. *Nat Rev Immunol* 3(9):710–720.
- Bardan A, Nizet V, Gallo RL (2004) Antimicrobial peptides and the skin. *Expert Opin Biol Ther* 4(4):543–549.
- Paulmann M, et al. (2012) Structure-activity analysis of the dermcidin-derived peptide DCD-1L, an anionic antimicrobial peptide present in human sweat. *J Biol Chem* 287(11):8434–8443.
- Cipáková I, Gasperik J, Hostenová E (2006) Expression and purification of human antimicrobial peptide, dermcidin, in *Escherichia coli*. *Protein Expr Purif* 45(2):269–274.
- Brogden KA, De Lucca AJ, Bland J, Elliott S (1996) Isolation of an ovine pulmonary surfactant-associated anionic peptide bactericidal for *Pasteurella haemolytica*. *Proc Natl Acad Sci USA* 93(1):412–416.
- Eissa A, Amodeo V, Smith CR, Diamandis EP (2011) Kallikrein-related peptidase-8 (KLK8) is an active serine protease in human epidermis and sweat and is involved in a skin barrier proteolytic cascade. *J Biol Chem* 286(1):687–706.
- Hessa T, et al. (2005) Recognition of transmembrane helices by the endoplasmic reticulum translocon. *Nature* 433(7024):377–381.
- Hessa T, et al. (2007) Molecular code for transmembrane-helix recognition by the SecE1 translocon. *Nature* 450(7172):1026–1030.
- Bechinger B, Sizon C (2003) Alignment and structural analysis of membrane polypeptides by 15N and 31P solid-state NMR spectroscopy. *Concepts Magn Reson* 18A:130–145.
- Bechinger B, Resende JM, Aisenbrey C (2011) The structural and topological analysis of membrane-associated polypeptides by oriented solid-state NMR spectroscopy: Established concepts and novel developments. *Biophys Chem* 153(2-3):115–125.
- Murzyn K, Róg T, Pasenkiewicz-Gierula M (2005) Phosphatidylethanolamine-phosphatidylglycerol bilayer as a model of the inner bacterial membrane. *Biophys J* 88(2):1091–1103.
- Yang B, Verkman AS (1997) Water and glycerol permeabilities of aquaporins 1-5 and MIP determined quantitatively by expression of epitope-tagged constructs in *Xenopus* oocytes. *J Biol Chem* 272(26):16140–16146.
- Kutzner C, Grubmüller H, de Groot BL, Zachariae U (2011) Computational electrophysiology: The molecular dynamics of ion channel permeation and selectivity in atomistic detail. *Biophys J* 101(4):809–817.
- Hill CP, Yee J, Selsted ME, Eisenberg D (1991) Crystal structure of defensin HNP-3, an amphiphilic dimer: Mechanisms of membrane permeabilization. *Science* 251(5000):1481–1485.
- Terwilliger TC, Weissman L, Eisenberg D (1982) The structure of melittin in the form I crystals and its implication for melittin's lytic and surface activities. *Biophys J* 37(1):353–361.
- Langs DA (1988) Three-dimensional structure at 0.86 Å of the uncomplexed form of the transmembrane ion channel peptide gramicidin A. *Science* 241(4862):188–191.
- Bechinger B (1997) Structure and functions of channel-forming peptides: Magainins, cecropins, melittin and alamethicin. *J Membr Biol* 156(3):197–211.
- Fox RO, Jr., Richards FM (1982) A voltage-gated ion channel model inferred from the crystal structure of alamethicin at 1.5-Å resolution. *Nature* 300(5890):325–330.
- Roux B (2002) Theoretical and computational models of ion channels. *Curr Opin Struct Biol* 12(2):182–189.
- Christensen B, Fink J, Merrifield RB, Mauzerall D (1988) Channel-forming properties of cecropins and related model compounds incorporated into planar lipid membranes. *Proc Natl Acad Sci USA* 85(14):5072–5076.
- Kagan BL, Selsted ME, Ganz T, Lehrer RI (1990) Antimicrobial defensin peptides form voltage-dependent ion-permeable channels in planar lipid bilayer membranes. *Proc Natl Acad Sci USA* 87(1):210–214.
- Bechinger B (2011) Insights into the mechanisms of action of host defence peptides from biophysical and structural investigations. *J Pept Sci* 17(5):306–314.
- Bechinger B, Lohner K (2006) Detergent-like actions of linear amphipathic cationic antimicrobial peptides. *Biochim Biophys Acta* 1758(9):1529–1539.
- Kralj JM, Hochbaum DR, Douglass AD, Cohen AE (2011) Electrical spiking in *Escherichia coli* probed with a fluorescent voltage-indicating protein. *Science* 333(6040):345–348.
- Kabsch W (2010) Integration, scaling, space-group assignment and post-refinement. *Acta Crystallogr D Biol Crystallogr* 66(Pt 2):133–144.
- Adams PD, et al. (2011) The Phenix software for automated determination of macromolecular structures. *Methods* 55(1):94–106.
- Zwart PH, et al. (2008) Automated structure solution with the PHENIX suite. *Methods Mol Biol* 426:419–435.
- Winn MD, et al. (2011) Overview of the CCP4 suite and current developments. *Acta Crystallogr D Biol Crystallogr* 67(Pt 4):235–242.
- Cowtan K (2006) The Buccaneer software for automated model building. 1. Tracing protein chains. *Acta Crystallogr D Biol Crystallogr* 62(Pt 9):1002–1011.
- Emsley P, Lohkamp B, Scott WG, Cowtan K (2010) Features and development of Coot. *Acta Crystallogr D Biol Crystallogr* 66(Pt 4):486–501.
- Murshudov GN, et al. (2011) REFMAC5 for the refinement of macromolecular crystal structures. *Acta Crystallogr D Biol Crystallogr* 67(Pt 4):355–367.
- Aisenbrey C, Bertani P, Bechinger B (2010) Solid-state NMR investigations of membrane-associated antimicrobial peptides. *Methods Mol Biol* 618:209–233.
- Michalek M, Salnikov ES, Werten S, Bechinger B (2013) Membrane interactions of the amphiphilic amino-terminus of huntingtin. *Biochemistry* 52(5):847–858.
- Angelova MI, Dimitrov DS (1986) Liposome electroformation. *Faraday Discuss Chem Soc* 81:303–311.
- Angelova M, Dimitrov D (1988) A mechanism of liposome electroformation. *Trends in Colloid and Interface Science II*, ed Degiorgio V (Springer, Berlin), pp 59–67.
- Angelova M (2000) Giant vesicles. *Perspectives in Supramolecular Chemistry*, eds Luisi PL, Walde P (Wiley-Interscience, Chichester, UK), 1st Ed, pp 27–36.
- Hess B, Kutzner C, Van der Spoel D, Lindahl E (2008) GROMACS 4: Algorithms for highly efficient, load-balanced, and scalable molecular simulation. *J Chem Theory Comput* 4:435–447.
- Klauda JB, et al. (2010) Update of the CHARMM all-atom additive force field for lipids: Validation on six lipid types. *J Phys Chem B* 114(23):7830–7843.
- Bussi G, Donadio D, Parrinello M (2007) Canonical sampling through velocity rescaling. *J Chem Phys* 126(1):014101.
- Essmann U, et al. (1995) A smooth particle mesh Ewald method. *J Chem Phys* 103:8577–8593.
- Hess B, Bekker H, Berendsen HJC, Fraaije JGEM (1997) LINCS: A linear constraint solver for molecular simulations. *J Comput Chem* 18:1463–1472.
- Feenstra KA, Hess B, Berendsen HJC (1999) Improving efficiency of large time-scale molecular dynamics simulations of hydrogen-rich systems. *J Comput Chem* 20:786–798.

Supporting Information

Song et al. 10.1073/pnas.1214739110

SI Materials and Methods

Crystallization and Structure Solution of the Dermcidin Peptide. The dermcidin peptide sequence (Fig. S1) was synthesized by the company Peptide2.0 (www.peptide2.com) to yield a product of >97% purity. For crystallization, the peptide was dissolved in 10 mM Hepes at a concentration of 50 mg/mL (~10 mM final concentration). Crystallization drops were prepared by mixing 400 nL of the peptide solution with the same amount of reservoir, and drops were incubated by vapor diffusion (sitting drops) under a variety of different conditions (800 conditions from Qiagen screens). Two conditions, both of which contained Zn-acetate, yielded crystals suitable for X-ray diffraction analysis. Crystals for X-ray diffraction were taken from a drop containing 0.2 M Zn(ac)₂, 0.1 M Na-cacodylate, 18% (wt/vol) PEG8000 at pH 6.5. Crystals were taken from the mother liquor and flash-frozen in liquid nitrogen without adding cryoprotectant. Data were collected at the Swiss Light Source, beamline PXII at 100 K and 20 eV above the theoretical Zn-edge (9.658 keV). Three-hundred sixty 1° images were collected at 2% beam intensity to generate a highly redundant dataset for single anomalous dispersion data processing. Diffraction data were processed with XDS/XSCALE (1). The structure was solved with the PHENIX program package (2) with Phaser (3) for heavy atom detection and Resolve (4) for initial solvent flattening. Solvent flattening was repeated by Pirate of the CCP4 suite (5) and a model with 85% completeness was built with Buccaneer (6). The final model was obtained after several rounds of manual rebuilding and refinement with Coot (7), REFMAC (8), and PHENIX (2). The structural geometry of all ligand structures was verified with Whatcheck (9); values are given in Table S1. Crystal structure images were generated with Pymol (Schrodinger). Sequence alignment of human dermcidin (DCD) (Fig. S1) was performed against sequences deposited to the current EXPASY (10) sequence database. Sequences similar to DCD were extracted with a PSI-BLAST (11) search. In addition, the secondary structure was predicted with PSIPRED (12).

Electrophysiology. Giant unilamellar vesicles (GUVs) were prepared by the electroformation method (13–15). A lipid mixture composed of diphytanoyl phosphatidylcholine (DPhPC)/cholesterol (9:1) dissolved in chloroform at a concentration of 10 mM (6.25 μL) was deposited on indium-tin-oxide (ITO) coated cover slides and allowed to dry. Two slides were connected to form a sealed chamber electrically connected to a voltage generator (33210A; Agilent Technologies). The lipid was rehydrated in approximately 2 mL 1 M sorbitol and GUV formation was carried out by application of a 3-V peak-to-peak AC voltage at a frequency of 5 Hz for 2 h at 20 °C.

A freestanding membrane was prepared by spreading a GUV on an aperture with a size of a few micrometers in diameter in a borosilicate chip (Port-a-Patch; Nanion Technologies). Two microliters of the GUV-containing solution were added to 6-μL buffer (1 M NaCl, 5 mM Hepes, pH 7.1) and a GUV was gently sucked onto the aperture by application of 15–40-mbar negative pressure. Spontaneous spreading of the GUV on the surface gave rise to a solvent-free membrane with resistances in the GΩ range.

After successful membrane formation, 50 μL of buffer were added and varying amounts of DCD-1L stock solution (100 μM) were added at a DC bias of 100 mV. Current traces were recorded with an Axopatch 200B amplifier (Axon Instruments). The analog output signals were filtered with a low-pass four-pole Bessel filter of 1 kHz and subsequently digitized by an A/D converter (Digidata 1322; Axon Instruments). The sampling rate

was 50 kHz. Data evaluation was performed with the pClamp 9 software package (Axon Instruments).

Solid-State NMR Spectroscopy. Samples for solid-state NMR spectroscopy were prepared by dissolving 4 mg of peptide and ~30 mg of lipid in TFE/water 50/50 vol/vol. Where appropriate ZnCl₂ was added in five- to ten-fold molar excess over the peptide. The solutions were mixed and carefully applied onto 20 ultra-thin cover glasses (6 × 11 mm; Paul Marienfeld) as described previously (16). Care was taken to remove all organic solvent in high vacuum. Thereafter, the samples were equilibrated at 93% relative humidity for several days.

An alternative preparation method consisted in mixing only the lipid in organic solvent and forming a dry film by evaporating the solvent and exposure to high vacuum (16, 17). Then 0.2 mL of water was added and a transparent vesicular suspension was prepared (five freeze/thaw cycles between liquid nitrogen and 310 K water bath). Thereafter 2 mg of peptide and 62 μg of ZnCl₂ were codissolved in 100 μL of water and added to the membrane vesicles, vortexed, and incubated for 4 h. The mixed lipid/peptide vesicles were applied onto glass plates, dried in air overnight, and equilibrated at 93% relative humidity.

Solid-state NMR spectra were recorded on a Bruker Avance wide-bore NMR spectrometer operating at 9.4 T. A commercial double-resonance solid-state NMR probe modified with flattened coils of dimensions 15 × 4 × 9 mm was used. Proton-decoupled ¹⁵N solid-state NMR spectra were acquired using a cross-polarization sequence and processed as described previously (18). The temperature was 310 K for 1-palmitoyl-2-oleoyl-*sn*-glycero-3-phosphoethanolamine (POPE)/1-palmitoyl-2-oleoyl-*sn*-glycero-3-phospho(1'-*rac*-glycerol) (POPG) and 295 K for 1-palmitoyl-2-oleoyl-*sn*-glycero-3-phosphocholine (POPC) and DPhPC/cholesterol 9:1 membranes. NH₄Cl (40.0 ppm) was used as an external reference corresponding to 0 ppm for liquid NH₃. An exponential apodization function corresponding to a line broadening of 50 Hz was applied before Fourier transformation.

Deuterium solid-state NMR spectra were recorded using a quadrupolar echo pulse sequence (19). The spectra were referenced relative to ²H₂O (0 Hz). An exponential apodization function corresponding to a line broadening of 500 Hz (for the ²H₃-peptide) or 30 Hz (for chain deuterated lipids) was applied before Fourier transformation. The deuterium order parameters are analyzed following reference (20).

To verify the alignment of the lipids, proton-decoupled ³¹P solid-state NMR spectra were recorded using a Hahn-echo pulse sequence as described previously (18) and referenced relative to 85% phosphoric acid (0 ppm).

Calculation of Orientational Restraints from the Solid-State NMR Spectra. To evaluate the peptide orientations that agree with the experimental spectra, a coordinate system was defined, with the tilt angle being the angle between the long axis of the helix and the membrane normal, and a pitch angle between membrane normal and the line within the arbitrary plane of peptide helical wheel projection (see Fig. S2B for angle definition). The calculations were performed using the ¹⁵N chemical shift main tensor elements for glycine (44, 65, 211) ppm (21) to agree with an isotropic chemical shift of 106.7 ppm and 74 kHz for the maximum quadrupolar splitting for the alanine ²H₃C-group at room temperature (22). The coordinates of DCD were from pdb:2ymk. By successively changing the tilt and pitch angles in (50 × 50 steps), the 3D topological space was systematically

screened and the corresponding ^{15}N chemical shift and quadrupolar splitting calculated (19). The restriction plot was calculated using azimuthal fluctuations of 18° Gaussian distribution and wobbling motions of 10° , similar to those which have been observed for other in-plane amphipathic helical peptides (e.g., refs. 23, 24). Contour plots mark the angular restrictions that agree with the experimental results.

Molecular Dynamics Simulations. All molecular dynamics (MD) simulations were performed with the GROMACS package, version 4.5 (25, 26) in combination with the CHARMM36 force field (27). Unless otherwise stated, the simulation temperature was 310 K. The protein, lipids, and water/ions were coupled separately to a temperature bath with the v-rescale method with a time constant of 0.1 ps (28). Short-range electrostatics were calculated with a cutoff of 1.3 nm. Long-range electrostatics were treated with the particle-mesh Ewald method (29, 30). Short-range Van der Waals (VdW) interactions were calculated explicitly up to a distance of 0.8 nm, beyond which a switch function was used to smoothly switch off the VdW interactions to reach zero at 1.2 nm. All bonds were constrained with the LINCS method (31). The time step was 2 fs for all-atom MD simulations and 4 fs for simulations with the virtual site model for hydrogen atoms (32), respectively.

The crystal structure of the DCD hexamer, as described in this study, was used to generate the initial configuration for our MD simulations. Specifically, the protein and six Zn^{2+} ions at the monomeric interfaces of the DCD oligomer were taken from the crystal structure, which was then embedded into a mixed bilayer of palmitoyloleoyl-phosphatidylethanolamine and palmitoyloleoylphosphatidylglycerol (POPE/POPG; 3:1) lipids, which resembles the composition of the bacterial cytoplasmic membrane (33). To test the tilting of DCD in various bilayer environments, additional simulations were carried out in dimyristoyl phosphatidylcholine (DMPC), dipalmitoyl phosphatidylcholine (DPPC), distearoyl phosphatidylcholine (DSPC), and diarachidonoyl phosphatidylcholine (DAPC) lipid bilayers. All membranes were generated with CHARMM-GUI (34).

The POPE/POPG bilayer consisted of 72 POPE and 24 POPG molecules in each bilayer leaflet, solvated by 13,938 TIP3P water molecules (35). Also, 82 Na^+ and 38 Cl^- ions were added to the simulation system resulting in an ionic strength of about 150 mM. The POPE/POPG lipids were first energy-minimized for 5,000 steps with the steepest descent algorithm, then equilibrated in an NVT ensemble at 310 K for 500 ps, while position restraints were applied ($1,000 \text{ kJ}\cdot\text{mol}^{-1}\cdot\text{nm}^{-2}$) on the lipid heavy atoms. Subsequently, the system was further equilibrated without any restraints under semi-isotropic Berendsen pressure coupling (36). The reference pressure was set to 1 bar and the pressure coupling time constant was 1.0 ps. After ~ 1 ns of simulation in the NPT ensemble, the area per lipid reached about 0.615 nm^2 . This configuration was adopted for additional 15 ns of NPAT simulation to further equilibrate the system. The GROMACS utility `g_membed` (37) was used to insert DCD into the lipid bilayer. By comparing the lateral pressures to those of pure lipids, we found that by removing nine lipid molecules, the differences between the lateral pressures of DCD-embedded and pure systems are smallest. Therefore, approximately nine lipid molecules were removed in each leaflet before insertion of the DCD oligomer. To test convergence, we used three different initial configurations of the lipid bilayer in our MD simulations by taking frames at various points of the equilibration simulation (taken at 13, 14, and 15 ns from the above lipids equilibration simulation). The antimicrobial peptide (AMP) assembled structure was thus inserted into three different membrane

microenvironments. The adoption of three independent initial simulation systems can reduce possible bias on the simulation results arising from the initial system setup. One of the resulting single-bilayer simulation systems is shown in Fig. S5 *A* and *B*.

Starting from the three independent systems described above, we first performed 5,000 steps of steepest descent energy minimization, then 10 ns of NPAT equilibration simulations with the heavy atoms of the protein and Zn^{2+} position restrained ($1,000 \text{ kJ}\cdot\text{mol}^{-1}\cdot\text{nm}^{-2}$). These equilibration simulations allowed water molecules to fill the interior of the DCD oligomer. Monitoring of the number of water molecules showed that it no longer increased after 7.5 ns. Subsequently, 250-ns simulations were performed for all of the three systems under NPAT conditions. In addition, we performed three corresponding simulations without any Zn^{2+} in the system to investigate the importance of Zn^{2+} for the stability of the X-ray structure.

To study whether the oligomer is ion conductive, we used the computational electrophysiology method (38). Structures were taken from the three single-patch simulations at 100 ns and the systems were duplicated in the Y direction. The virtual-site model was used for peptides and lipids (32). A transmembrane electric field was generated by sustaining a slight imbalance of ions in the two compartments thus formed during the simulation by ion exchanges. This ionic imbalance evoked an electrostatic potential gradient across the two bilayers of ± 200 – 800 mV in multiple simulations, as determined by double integration of Poisson's equation (38). Under these conditions, six independent 200-ns production simulations were performed with a time step of 4 fs in the NPAT ensemble. The simulation system of the double-bilayer setup is shown in Fig. S5C.

To run simulations under conditions similar to our electrophysiological experiments, we also carried out computational electrophysiology simulations, in which 506 Cl^- and 594 Na^+ ions were included in the double-patch system, which resulted in an ion concentration of ~ 1 M. Here again, an equal number of Cl^- ions were included in the two compartments, and a small difference of Na^+ ions between compartment I and II was sustained during the simulation, which generated transmembrane potentials fluctuating in the range from ~ 20 to 300 mV. Subsequently, five independent simulations were performed to monitor ion permeation.

Altogether, we performed five independent double-patch simulations with 1M NaCl (200 ns each), six independent double-patch simulations with 150 mM NaCl (200 ns each), four single-patch simulations with various lipids (>250 ns each), three independent single-patch simulations (250 ns each), and three independent single-patch simulations in the absence of Zn^{2+} (200 ns each). Simulation images were generated with Pymol (Schrodinger).

Pore Size Analysis. To good approximation, the conductance of membrane channels is proportional to their channel cross-sectional area; i.e., it varies with the square of the difference of the pore radii (39). Due to the fact that the channel is composed of units of antiparallel dermcidin dimers, it is reasonable to assume that channel-forming oligomers would consist of an even number of 4, 6, 8, etc., peptides. By using the peptide-peptide docking software `m-Zdock` (40), which is specialized for generating symmetrical pores, we find that (i) tetrameric assemblies are not capable of forming a pore, and (ii) peptide octamers with their hydrophobic face toward the membrane would have a pore diameter of about ~ 11 Å. According to our calculations, this pore size would lead to a conductance above 0.5 nS. This value is more than five times higher than that found in our experiments. Higher-order oligomers could be expected to have a further increased conductance. Hence, lower- or higher-order dermcidin channels are not a likely explanation for our experimentally measured channel currents.

1. Kabsch W (2010) Integration, scaling, space-group assignment and post-refinement. *Acta Crystallogr D Biol Crystallogr* 66(Pt 2):133–144.
2. Adams PD, et al. (2011) The Phenix software for automated determination of macromolecular structures. *Methods* 55(1):94–106.
3. Read RJ, McCoy AJ (2011) Using SAD data in Phaser. *Acta Crystallogr D Biol Crystallogr* 67(Pt 4):338–344.
4. Zwart PH, et al. (2008) Automated structure solution with the PHENIX suite. *Methods Mol Biol* 426:419–435.
5. Winn MD, et al. (2011) Overview of the CCP4 suite and current developments. *Acta Crystallogr D Biol Crystallogr* 67(Pt 4):235–242.
6. Cowtan K (2006) The Buccaneer software for automated model building. 1. Tracing protein chains. *Acta Crystallogr D Biol Crystallogr* 62(Pt 9):1002–1011.
7. Emsley P, Lohkamp B, Scott WG, Cowtan K (2010) Features and development of Coot. *Acta Crystallogr D Biol Crystallogr* 66(Pt 4):486–501.
8. Murshudov GN, et al. (2011) REFMAC5 for the refinement of macromolecular crystal structures. *Acta Crystallogr D Biol Crystallogr* 67(Pt 4):355–367.
9. Schwede T, Kopp J, Guex N, Peitsch MC (2003) SWISS-MODEL: An automated protein homology-modeling server. *Nucleic Acids Res* 31(13):3381–3385.
10. Gasteiger E, et al. (2003) ExPASy: The proteomics server for in-depth protein knowledge and analysis. *Nucleic Acids Res* 31(13):3784–3788.
11. Altschul SF, Gish W, Miller W, Myers EW, Lipman DJ (1990) Basic local alignment search tool. *J Mol Biol* 215(3):403–410.
12. Jones DT (1999) Protein secondary structure prediction based on position-specific scoring matrices. *J Mol Biol* 292(2):195–202.
13. Angelova MI, Dimitrov DS (1986) Liposome electroformation. *Faraday Discuss Chem Soc* 81:303–311.
14. Angelova M, Dimitrov D (1988) A mechanism of liposome electroformation. *Trends in Colloid and Interface Science II*, ed Degiorgio V (Springer, Berlin), pp 59–67.
15. Angelova M (2000) *Giant vesicles. Perspectives in Supramolecular Chemistry*, eds Luisi PL, Walde P (Wiley-Interscience Chichester, UK), 1st Ed, pp 27–36.
16. Aisenbrey C, Bertani P, Bechinger B (2010) Solid-state NMR investigations of membrane-associated antimicrobial peptides. *Methods Mol Biol* 618:209–233.
17. Aisenbrey C, Michalek M, Salnikov E, Bechinger B (2013) *Lipid-Protein Interactions: Methods and Protocols (Methods in Molecular Biology)*, ed Jh K (Springer, New York).
18. Salnikov ES, et al. (2011) Structure and alignment of the membrane-associated antimicrobial peptide arenicin by oriented solid-state NMR spectroscopy. *Biochemistry* 50(18):3784–3795.
19. Aisenbrey C, Bechinger B (2004) Tilt and rotational pitch angle of membrane-inserted polypeptides from combined 15N and 2H solid-state NMR spectroscopy. *Biochemistry* 43(32):10502–10512.
20. Bechinger B, Salnikov ES (2012) The membrane interactions of antimicrobial peptides revealed by solid-state NMR spectroscopy. *Chem Phys Lipids* 165(3):282–301.
21. Salnikov E, Bertani P, Raap J, Bechinger B (2009) Analysis of the amide (15N) chemical shift tensor of the C(α) tetrasubstituted constituent of membrane-active peptides, compared to those of di- and tri-substituted proteinogenic amino acid residues. *J Biomol NMR* 45(4):373–387.
22. Batchelder LS, Niu CH, Torchia DA (1983) Methyl reorientation in polycrystalline amino acids and peptides: A deuteron NMR spin-lattice relaxation study. *J Am Chem Soc* 105:2228–2231.
23. Strandberg E, Esteban-Martín S, Salgado J, Ulrich AS (2009) Orientation and dynamics of peptides in membranes calculated from 2H-NMR data. *Biophys J* 96(8):3223–3232.
24. Michalek M, Salnikov ES, Werten S, Bechinger B (2013) Membrane interactions of the amphipathic amino-terminus of huntingtin. *Biochemistry* 52(5):847–858.
25. Berendsen HJC, van der Spoel D, van Druenen R (1995) GROMACS: A message-passing parallel molecular dynamics implementation. *Comput Phys Commun* 91:43–56.
26. Hess B, Kutzner C, van der Spoel D, Lindahl E (2008) GROMACS 4: Algorithms for highly efficient, load-balanced, and scalable molecular simulation. *J Chem Theory Comput* 4:435–447.
27. Klauda JB, et al. (2010) Update of the CHARMM all-atom additive force field for lipids: Validation on six lipid types. *J Phys Chem B* 114(23):7830–7843.
28. Bussi G, Donadio D, Parrinello M (2007) Canonical sampling through velocity rescaling. *J Chem Phys* 126(1):014101.
29. Darden T, York D, Pedersen L (1993) Particle mesh Ewald: An N · log (N) method for Ewald sums in large systems. *J Chem Phys* 98:10089.
30. Essmann U, et al. (1995) A smooth particle mesh Ewald method. *J Chem Phys* 103:8577–8593.
31. Hess B, Bekker H, Berendsen HJC, Fraaije JGEM (1997) LINCS: A linear constraint solver for molecular simulations. *J Comput Chem* 18:1463–1472.
32. Feenstra KA, Hess B, Berendsen HJC (1999) Improving efficiency of large time-scale molecular dynamics simulations of hydrogen-rich systems. *J Comput Chem* 20:786–798.
33. Murzyn K, Róg T, Pasenkiewicz-Gierula M (2005) Phosphatidylethanolamine-phosphatidylglycerol bilayer as a model of the inner bacterial membrane. *Biophys J* 88(2):1091–1103.
34. Jo S, Kim T, Iyer VG, Im W (2008) CHARMM-GUI: A web-based graphical user interface for CHARMM. *J Comput Chem* 29(11):1859–1865.
35. Jorgensen WL, Chandrasekhar J, Madura JD, Impey RW, Klein ML (1983) Comparison of simple potential functions for simulating liquid water. *J Chem Phys* 79:926–935.
36. Berendsen HJC, Postma JPM, Van Gunsteren WF, DiNola A, Haak JR (1984) Molecular dynamics with coupling to an external bath. *J Chem Phys* 81:3684–3690.
37. Wolf MG, Hoefling M, Aponte-Santamaria C, Grubmüller H, Groenhof G (2010) g_membed: Efficient insertion of a membrane protein into an equilibrated lipid bilayer with minimal perturbation. *J Comput Chem* 31(11):2169–2174.
38. Kutzner C, Grubmüller H, de Groot BL, Zachariae U (2011) Computational electrophysiology: The molecular dynamics of ion channel permeation and selectivity in atomistic detail. *Biophys J* 101(4):809–817.
39. Hille B (2001) *Ion channels of excitable membranes* (Sinauer, Sunderland, MA), 3rd Ed.
40. Pierce B, Tong W, Weng Z (2005) M-ZDOCK: A grid-based approach for Cn symmetric multimer docking. *Bioinformatics* 21(8):1472–1478.

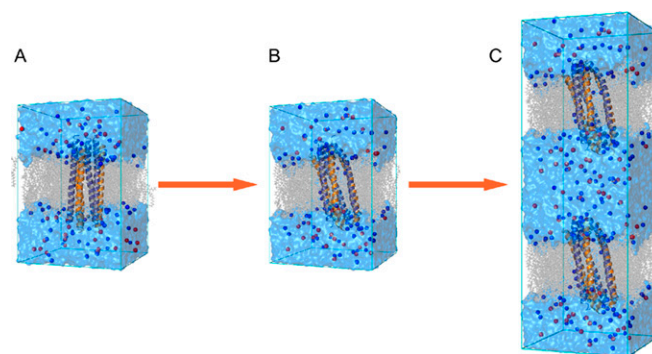


Fig. S5. Model system used in the MD simulations. (A) The initial simulation system, which contains the X-ray structure of DCD (orange and deep blue cartoon helices), the POPE/POPG (3:1) lipids bilayer (gray sticks), water box (light blue surface), Na^+ (blue spheres), and Cl^- (red spheres) ions. (B) The MD conformation after 100-ns simulation, which was then duplicated in the membrane normal direction to form the double-patch simulation system for the computational electrophysiology simulations (C).

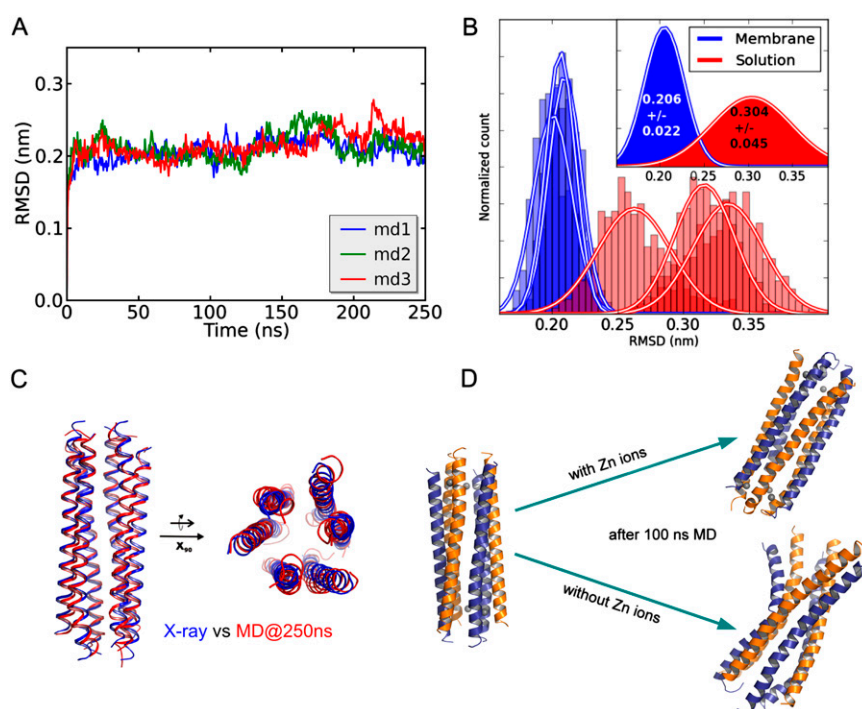
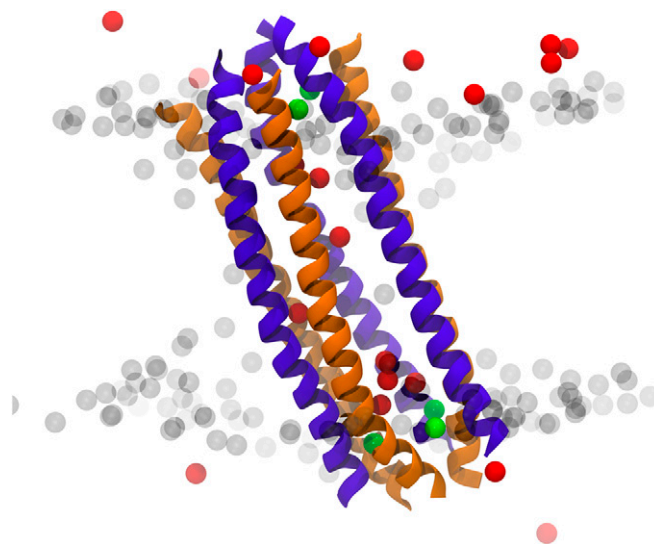


Fig. S6. Stability of the X-ray structure in MD simulations. (A) Evolution of the RMSD of the DCD oligomer (alpha carbon atoms) in the POPE/POPG bilayer during the 250-ns MD simulations. Results are calculated from three independent simulations. (B) Comparison of the stability of the DCD X-ray structure in membrane (blue) and solution (red). On average, the oligomer structure deviates from the X-ray structure by about 1 Å more in solution than in the membrane. Therefore, the X-ray channel structure is relatively more stable in a membrane environment. (C) Side and top views of the comparison between the X-ray structure (in blue) and the MD conformation at 250 ns (in red), respectively. The MD conformation was fitted onto the X-ray structure, which was then used as the starting structure for additional computational electrophysiology simulations. (D) Importance of Zn^{2+} ions for the stability of the oligomer channel. Starting with the initial oligomer structure in the single-patch MD simulations, the channel structure is preserved in the MD simulations in the presence of six Zn^{2+} ions. By contrast the channel structure evolves strong distortions in the absence of Zn^{2+} .

Table S1. Data collection and refinement statistics

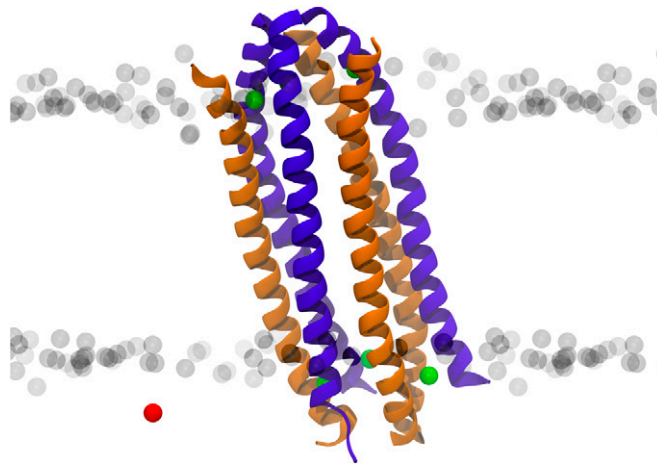
		Dermcidin*
Data collection		
Space group		C2
Cell dimensions		
<i>a</i> , <i>b</i> , <i>c</i> (Å)		76.35, 50.72, 45.73
α , β , γ (°)		90, 117.74, 90
Resolution (Å)		33–2.5 (2.66–2.5)
R_{merge}		0.02 (0.51)
$I/\sigma I$		17 (2.95)
Completeness (%)		98.8 (96.8)
Redundancy		7.2 (7.1)
Wavelength		1.2795
Refinement		
Resolution (Å)		33–2.5 (2.56–2.5)
No. reflections		5189
$R_{\text{work}}/R_{\text{free}}$		0.21/0.27 (0.23/0.27)
No. atoms (all)		
Protein		980
Ions (Zn ²⁺)		6
Water		20
<i>B</i> factors		
Protein		27.7
Ions (Zn ²⁺)		70.5
Water		31.7
Root-mean square. deviations		
Bond lengths (Å)		0.02
Bond angles (°)		2.0

*Values in parentheses are for highest-resolution shell.



Movie S1. Multiion permeation mechanism across DCD driven by transmembrane electric fields present across bacterial membranes. Ions enter sideways into the pore across the lateral openings that occur at the trimeric interfaces. Anion transfer across the inner pore usually involves single ion "hopping" steps. Near the channel exit, anions accumulate to form a cluster of three to four ions. Ions exiting the channel are often observed to be translocated by multiion "knock-on" effects, by which anions are transferred to the bulk solution.

[Movie S1](#)



Movie S2. Single anion followed on its pathway through the DCD channel, driven by a transmembrane electric field. Simulations settings are identical to [Movie S1](#), but only one permeating ion is shown to clearly illustrate the permeation pathway.

[Movie S2](#)